ACSNANO

www.acsnano.org

# Vitrified Metal–Organic Framework Composite Electrolyte Enabling Dendrite-Free and Long-Lifespan Solid-State Lithium Metal Batteries

Shouxiang Liu, Guangshen Jiang,* Yimao Wang, Chengyang Liu, Tongyang Zhang, Yanyan Wei,* and Baigang An*

Cite This: https://doi.org/10.1021/acsnano.3c11725

Read Online

ACCESS | Metrics & More | Article Recommendations | Supporting Information

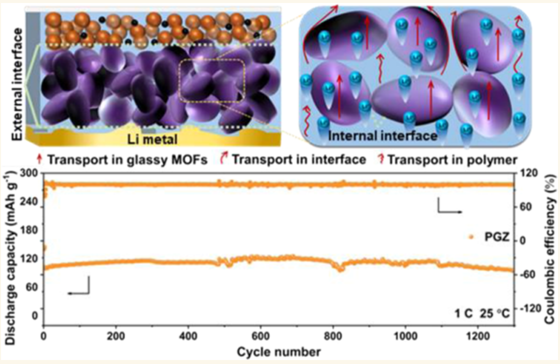

**ABSTRACT:** **Solid-state lithium metal batteries (LMBs) are still plagued with low ionic conductivity and inferior interfacial contact, which hinder their practical implementation. Herein, a quasi-solid-state composite electrolyte, poly(1,3-dioxolane) (PDOL)/glassy ZIF-62 (PGZ) with fast ion transport and intimate interface contact, is fabricated via in situ polymerization. The in situ polymerization of DOL in an electrolyte matrix not only improves the exterior interface between electrolyte/electrode but also optimizes the inner interfaces among glassy particles, rendering PGZ as an uninterrupted ionic conductor. Moreover, PGZ inherits the superior ionic conductivity and the robust dendrite prohibition of glassy MOFs originating from their grain-boundary-free nature, isotropy, and abundant groups containing N species. As expected, our proposed PGZ exhibits a prominent ionic conductivity of $6.3 \times 10^{-4}$ S cm$^{-1}$ at 20 °C. Li|PGZ|LiFePO$_4$ delivers an outstanding rate performance (103 mAh g$^{-1}$ at 4C) and a stable cycling capacity (118 mAh g$^{-1}$ at 1C over 1000 cycles). PGZ also presents excellent low-temperature cycling performance with 75 mAh g$^{-1}$ for 480 cycles at −20 °C and excellent flame retardance. Even at a high loading of 12.1 mg cm$^{-2}$, it can still discharge at 140 mAh g$^{-1}$ for 100 cycles. Hence, PGZ prepared via in situ polymerization holds enormous prospects as a solid-state electrolyte for high-performance and safe LMBs.**

KEYWORDS: *metal–organic frameworks, MOF glass, ZIF-62, solid-state electrolyte, in situ polymerization*

## 1. INTRODUCTION

The thirst for high-energy-density and high-safety lithium metal batteries inspires enormous endeavors in exploiting advanced solid-state electrolytes (SSEs),[1−3] while SSEs are still subject to low ion conductivity and severe interface issues.[4] Among them, composite electrolytes, integrated with the robust rigidity and ionic conduction of inorganics and the good flexibility of polymers, are demonstrated as competitive candidates for solid-state lithium metal batteries (SLMBs).[5,6] As one of the booming inorganic parts of composite electrolytes, metal–organic frameworks (MOFs), linked by metal ions and organic ligands, are electronically insulating and readily processable.[7] Moreover, coordination chemistry and reticular design principles offer unlimited possibilities for extending the structural diversity and properties of MOFs,[8] meaning that MOFs can be modulated through the customization of chemical components and network topologies according to task-specific demands.[9] These features empower them as a competitive inorganic matrix for composite electrolytes.

As attractive derivatives of crystalline MOFs, glassy MOFs rely on their grain-boundary-free nature and isotropy and thus have no transport impedance among boundaries with the same migration rate along all directions for fast ion conduction besides common attributes with MOF crystals.[10−12] Our pioneering work has confirmed the effectiveness of MOF glass as an SSE substrate conducting Li$^+$ through structural defects

Received: November 23, 2023
Revised: May 10, 2024
Accepted: May 21, 2024

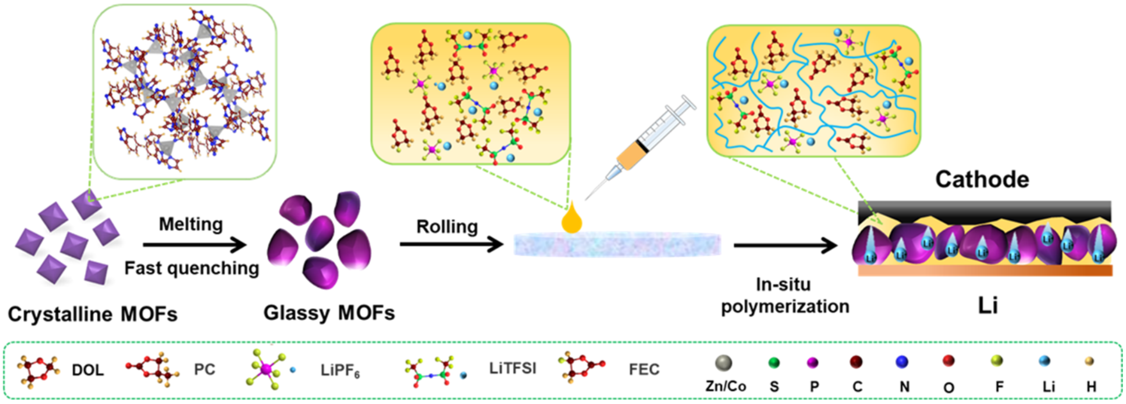

**Figure 1.** Schematic synthesis route of PGZ.

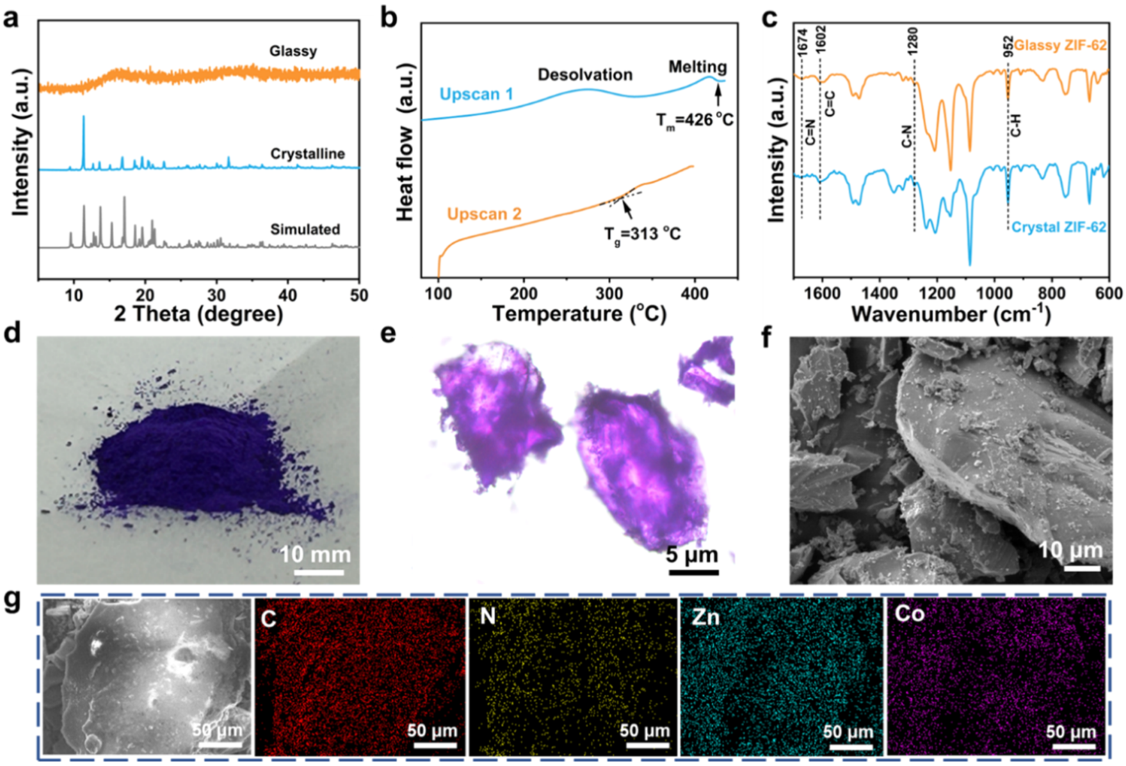

**Figure 2.** (a) XRD patterns of glassy ZIF-62, crystalline ZIF-62, and simulated ZIF-62. (b) DSC upscans of crystalline ZIF-62. (c) IR spectra of glassy ZIF-62 and crystalline ZIF-62. (d−f) Photo, optical microscopy, and SEM images of glassy ZIF-62 after grinding. (g) EDS mappings of glassy ZIF-62.

and segment motion in itself with a cycling capacity of 104 mAh g$^{-1}$ at 1C for 500 cycles.[13] Like inorganic electrolytes, nevertheless, the unfavorable interfacial contacts of glassy MOF including the interface among inorganic particles (denoted as the internal interface) and the interface between SSE and electrodes (denoted as the external interface) obstruct ion transport. To improve the situation above, the as-synthesized polymers are widely appreciated by many researchers owing to their high ionic conductivity and flexibility. For instance, glassy titanium alkoxide networks (TANs) were incorporated with poly(ethylene oxide) (PEO) and delivered a capacity of 128.7 mAh g$^{-1}$ at 0.5C.[13,14] Despite a certain enhancement of their rate performance, there is still large room to boost due to the presence of insufficient interior interface contact generated by the worse infiltrability of viscous polymers ahead of the battery assembly. Hence, rationally optimizing interior and exterior interfaces simultaneously is one of the top priorities to enhance the comprehensive electrochemical performance of solid-state LMBs.

Herein, we integrate polymers into MOF glass membranes via an in situ polymerization strategy and achieve the prominent performance of solid-state batteries. Like other MOF glasses, the ZIF-62(Zn,Co) (denoted ZIF-62) glass film bears the excellent ionic conductivity generated by grain-boundary-free nature, isotropy, abundant groups containing N species and mechanical robustness entitled by glass attribute, ensuring high ion migration and splendid dendrite suppression. The in situ introduction of flexible poly(1,3-dioxolane) (denoted PDOL) can fill in the interspace among MOF glass particles and gaps between SSE and electrodes, which renders the whole SSE to be a continuous heterophase for uninterrupted ion conduction. As a consequence, our proposed

https://doi.org/10.1021/acsnano.3c11725

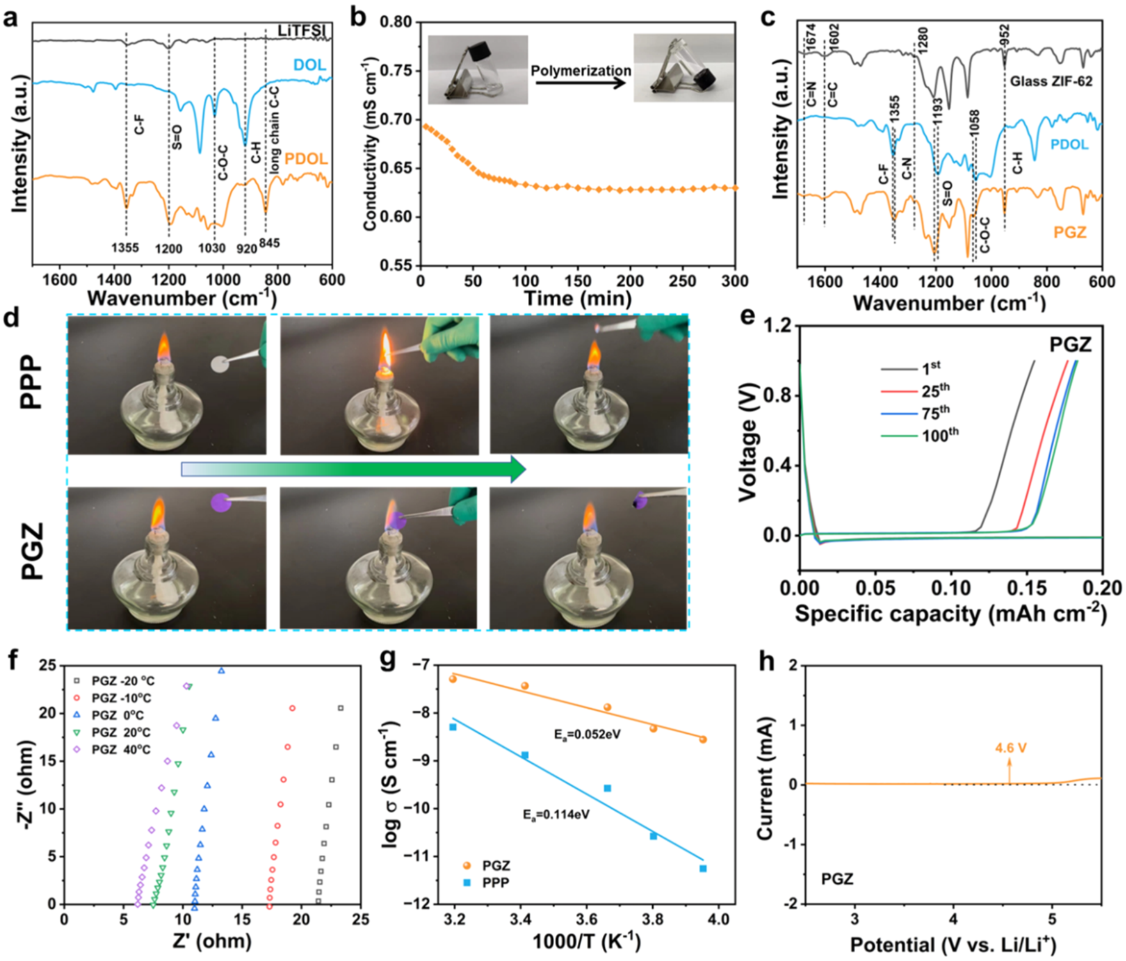

**Figure 3.** (a) IR spectra of PDOL, DOL, and LiTFSI. (b) Evolution of the ionic conductivity during the gelation process (inset: photograph of the DOL gel process). (c) IR spectra of glassy ZIF-62, PDOL, and PGZ. (d) Combustion behaviors of the PGZ film and PP separator. (e) The corresponding typical charge/discharge curves of Li|Cu cells with PGZ. (f) Nyquist plots for PGZ from −20 to 40 °C. (g) Arrhenius plots of PGZ and PPP. (h) LSV of the Li|PGZ|SS cell.

composite electrolyte PDOL/glassy ZIF-62 (denoted PGZ) displays an outstanding ionic conductivity of $6.3 \times 10^{-4}$ S $cm^{-1}$ at 20 °C and runs for 1800 h at 0.3 mA $cm^{-2}$ in the symmetric cell Li|PGZ|Li. Full cells Li|PGZ|$LiFePO_4$ deliver a good rate performance of 103 mAh $g^{-1}$ at 4C and a stable cycling capacity of 118 mAh $g^{-1}$ over 1000 cycles at 1C. PGZ also presents prominent low-temperature cycling performance and flame retardance. Hence, the in situ integration of PDOL into glassy MOF membranes demonstrates a huge prospect as a solid-state electrolyte for high-performance and safe LMBs and holds immense commercial potential.

## 2. RESULTS AND DISCUSSION

The grain boundary-free and isotropic nature of glass materials and the chemical diversity of coordination polymers empower glassy MOFs as promising electrolyte matrices for solid-state batteries.[15,16] Although the rigidity of MOF glass can intensify dendrite suppression, this property gives rise to poor interfacial contact with the electrodes. Incorporating polyacrylate,[17] polyether,[18,19] polycarbonate,[20] and poly(vinylidene fluoride-*co*-hexafluoropropylene) (PVDF-HFP)[21] into inorganic electrolytes can improve the dilemma, as verified by many previous reports. Nevertheless, this approach cannot optimize the poor inner interface contact generated by the worse infiltrability of vicious polymers and the inferior exterior interface contact induced by ex situ polymerization before battery assembly. Inspired by this concept, we triumphaly in situ fabricate composite solid electrolytes, i.e., MOF glass-based electrolyte PGZ. Initially, vitrified ZIF-62 is obtained through melting–quenching treatment from its crystalline counterpart and undergoes a rolling process into a glassy MOF film (Figure 1). When the battery is assembled, the as-prepared solution containing the DOL monomer, lithium bis(trifluoromethanesulphonyl)imide (LiTFSI), and fluoroethylene carbonate (FEC) is dropped onto the vitrified MOF membrane and infiltrates into the gaps inside the film. Under the initiation of $LiPF_6$ dissolved in propylene carbonate (PC), the infiltrated DOL in voids among particles and between electrolyte/electrodes is polymerized, and the formed polymer fills in them. The as-obtained PGZ hybrid electrolyte bears a continuous heterophase for uninterrupted ion conduction by ZIF-62 glass and amorphous domains in PDOL. This means that introducing PDOL via in situ polymerization into the glassy MOF film synchronously improves the situation of the interior and exterior interface contacts.[22,23] As expected, the PGZ composite electrolyte inherits superior ionic conductivity, robust dendrite prohibition of glassy MOFs, and favorable interfacial contact from PDOL with splendid adaptability.

Generally, MOF glass is constructed via a fast melting–quenching process from their crystalline counterparts.[24] In our work, crystalline ZIF-62 is synthesized by a solvothermal approach. X-ray diffraction (XRD) patterns record the vitrification transition of ZIF-62. The crystalline sample has a pattern consistent with the simulated one, while all of the original characteristic peaks disappear in the vitrified sample with only one broad peak located at 16.5°, illustrating the successful achievement of glassy ZIF-62 (Figure 2a). To further monitor the vitrification behavior of ZIF-62, the differential scanning calorimetry (DSC) method was conducted. In the first upscan, the crystalline ZIF-62 subsequently undergoes complete desolvation and melting at 265 and 426 °C, respectively (Figure 2b). The vitrification transformation is observed at 313 °C ($T_g$) during the second upscan, which is in agreement with the earlier reports.[25] This result also demonstrates the occurrence of vitrification. As shown in Figure S1, DMF desolvation occurs at 200 °C, and decomposition starts at 600 °C for ZIF-62. This outstanding thermal stability stems from the intensive coordination interaction between the metal center and organic ligands including imidazole and benzimidazole. After vitrification, glassy ZIF-62 has parallel Fourier transform infrared (FTIR) spectroscopy with the crystalline sample despite its phase change (Figure 2c). In detail, the vitrified sample succeeds the vibrations peaks of C═N (1674 $\mathrm{cm^{-1}}$), C═C (1602 $\mathrm{cm^{-1}}$), C−N (1280 $\mathrm{cm^{-1}}$), and C−H (952 $\mathrm{cm^{-1}}$) from the imidazole and benzimidazole rings of the crystalline one,[26,27] implying that no chemical reaction occurs during heat treatment. The intensity change of peak at 1150 $\mathrm{cm^{-1}}$ may be caused by structural tortuosity and deformation of the entire crystal structure as well as local molecular motion during the vitrification process and thus induce changes in the chemical environment with some enhanced bond vibrations and some restricted bond vibrations. The as-obtained ZIF-62 glass presents a purple powder after grinding (Figure 2d) and transparent and glassy blocks under optical microscopy (Figure 2e). In Figure 2f, the irregular blocks are further observed by scanning electron microscopy (SEM). Energy dispersive spectra (EDS) mappings display that elements C, N, Zn, and Co are homogeneously distributed in glassy ZIF-62, as shown in Figure 2g. According to the $N_2$ adsorption/desorption test, crystalline ZIF-62 has an adsorption amount of 8.7 $\mathrm{cm^3\ g^{-1}}$ (STP) with a Brunauer−Emmett−Teller (BET) surface area of 10.0 $\mathrm{m^2\ g^{-1}}$, whereas ZIF-62 glass bears a lower adsorption amount of 7.6 $\mathrm{cm^3\ g^{-1}}$ (STP) with a lower BET surface area of 9.0 $\mathrm{m^2\ g^{-1}}$ (Figure S2). This volumetric contraction phenomenon stems from the structural deformation and densification after vitrification,[13,16] which is the cause of short-range disorder for glass materials.[28]

The polymerization of DOL with LiTFSI was investigated in depth. After polymerization, the vibration intensity of C−H (920 $\mathrm{cm^{-1}}$) decreases significantly, the C−O−C band (1030 $\mathrm{cm^{-1}}$) shifts, and a new peak located at 845 $\mathrm{cm^{-1}}$ representing long-chain C−C emerges compared with the pure DOL monomer[29] (Figure 3a), corroborating the occurrence of polymerization. In the PDOL sample, the vibration peaks of C−F (1355 $\mathrm{cm^{-1}}$) and S═O (1200 $\mathrm{cm^{-1}}$) ascribed to LiTFSI are observed;[30] however, the S═O band shifts to a lower wavenumber (1193 $\mathrm{cm^{-1}}$) compared with pure LiTFSI, verifying that PDOL can interact with $\mathrm{TFSI^-}$ and facilitates $\mathrm{Li^+}$ dissociation.[31] In contrast with unpolymerized DOL, new peaks emerge in PDOL, as confirmed by $^1$H nuclear magnetic resonance ($^1$H NMR) analysis (Figure S3), which is in accordance with the structure of the reported PDOL.[32] The number-average molecular weight determined by chromatography gel permeation chromatography (GPC) is approximately 3203 $\mathrm{g\ mol^{-1}}$ with a low dispersibility index of 1.5 (Figure S4). As shown in Figure 3b, the ionic conductivity decreases over time until 150 min, meaning that the polymerization basically completes. The inset of Figure 3b also shows that the primitive LiTFSI/DOL solution turns into a transparent solid product under initiation. To ensure full polymerization, we leave 24 h to cells at ambient temperature before the test. The FTIR spectra of the composite electrolyte PGZ were also examined. PGZ keeps the characteristic bands C═N (1674 $\mathrm{cm^{-1}}$), C═C (1602 $\mathrm{cm^{-1}}$), C−N (1280 $\mathrm{cm^{-1}}$), and C−H (952 $\mathrm{cm^{-1}}$) of ZIF-62 glass;[26,27] the peak positions of C−F (1355 $\mathrm{cm^{-1}}$) and S═O (1190 $\mathrm{cm^{-1}}$) ascribed to LiTFSI and C−O−C (1058 $\mathrm{cm^{-1}}$) from PDOL are retained despite their slight shifts (Figure 3c). These results demonstrate that ZIF-62 glass has intensive interactions with LiTFSI and PDOL.

According to the formula of our designed QSSE, the proportion of vitrified ZIF-62 is about 50 wt %, and the proportion of PDOL is about 25 wt % in PGZ. The liquid content of QSSE is about 16.17 wt %, as determined by thermal gravimetric analysis (TGA, Figure S5). The composite electrolyte PGZ appears purple with a thickness of ∼70 μm and can be bent, folded at 180°, and then flattened into an intact film, preliminarily demonstrating its good flexibility (Figure S6a,b). As shown in Figure S6c, the glass MOF film is relatively dense and flat overall. The flame retardancy of the QSSE is an important index to evaluate its battery safety. As shown in Figure 3d, a commercial polypropylene (PP) separator promptly burns out with a dazzling light. On the contrary, once the ignited PGZ film is withdrawn from fire, the flame quickly extinguishes without the following combustion. This sharp contrast evidently substantiates the excellent fire resistance of PGZ due to the generated N species from the imidazole ring and benzimidazole.[33,34] On the other hand, PGZ produces certain nitrogen-containing free radicals at high temperatures, which can inhibit the chain reaction of free radicals and delay the combustion of materials; during the combustion process, on the other hand, ZIF-62 can generate some noncombustible gases, such as $N_2$, diluting the concentration of the combustible substance and the oxygen in the air.[35] Therefore, the implementation of PGZ into LMBs can enhance their security.

Glassy ZIF-62 is prepared into a membrane in advance for in situ polymerization, which can effectively resolve the agglomeration of inorganics happening in the traditional solution coblending method. To probe the optimal amount of PDOL precursors containing LiTSFI and the initiator, the ionic resistances of composite electrolytes with various volumes of precursors after polymerization were analyzed. With increasing precursor volume, the corresponding resistance decreases, and their differences become narrow (Figure S7). An optimized volume of DOL (30 μL) is thus selected for the subsequent studies. The Coulombic efficiency (CE) was examined in the asymmetric cells with the configuration of Li‖Cu. The PGZ cell displays an initial CE of 75.65% at 0.2 $\mathrm{mA\ cm^{-2}}$ and 0.2 $\mathrm{mAh\ cm^{-2}}$, and the subsequent CE basically remains at ∼90% after 100 cycles (Figure S8a). The PGZ cell has small nucleation overpotential (e.g., 29 mV), and their plating/stripping voltage curves are always steady (Figure 3e), signifying the preeminent stability of the solid electrolyte interface (SEI) film, whereas the initial CE is 50% for the control group polymerized PP (PPP) cell and dramatically

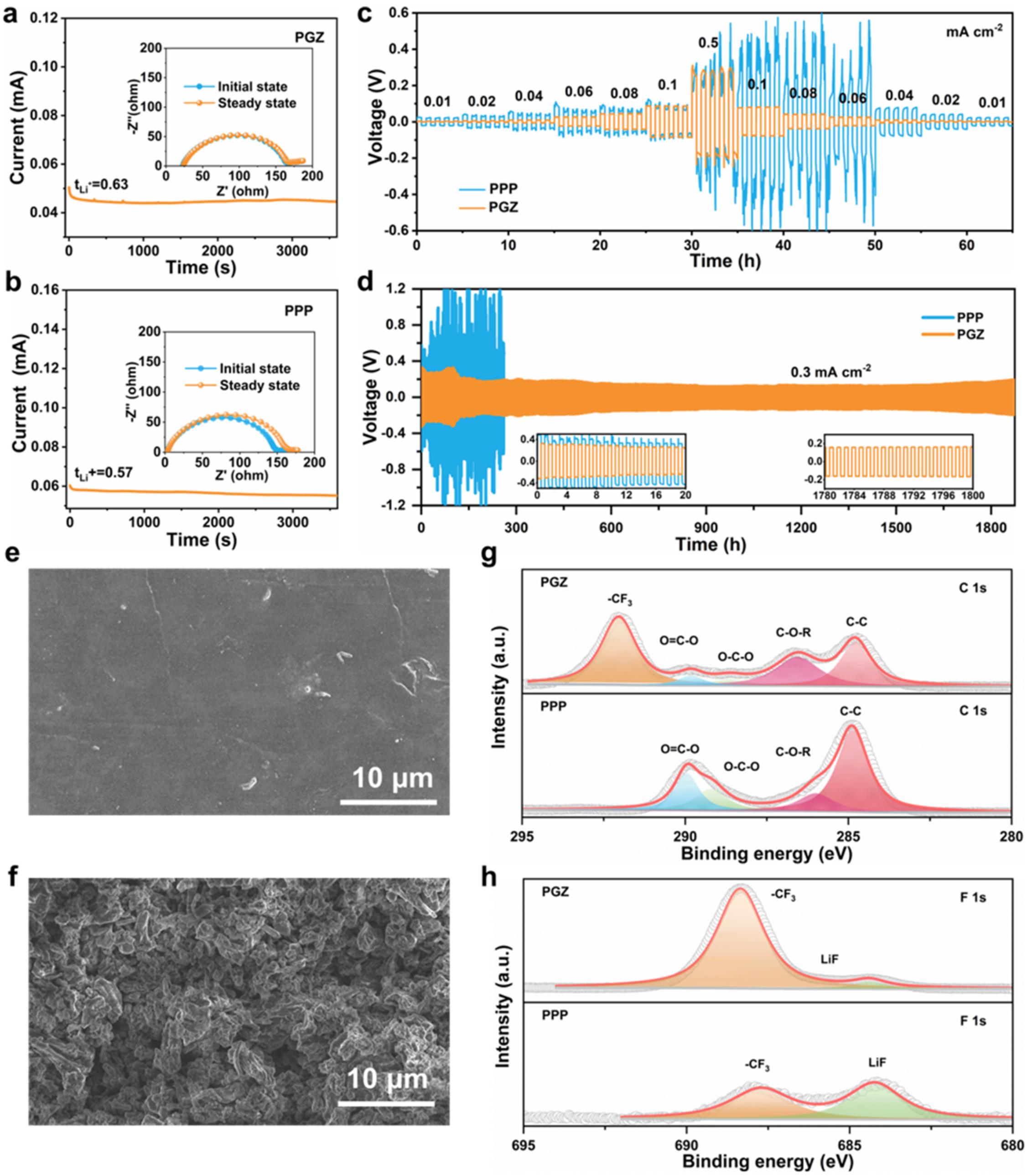

**Figure 4.** (a, b) Current−time curves of Li|PGZ|Li and Li|PPP|Li symmetric cells at 10 mV of polarization (inset: EIS at initial and steady states), respectively. (c) Rate performance of Li plating/stripping for Li|PGZ|Li and Li|PPP|Li cells. (d) Cycling stability of Li plating/stripping for Li|PGZ|Li and Li|PPP|Li cells at 0.3 mA cm$^{-2}$. (e, f) SEM images of Li anodes against PGZ and PPP after plating/stripping tests, respectively. (g, h) XPS analysis of C 1s and F 1s spectra of PGZ and PPP after cycling in Li/Li symmetric batteries.

decreases to 10% from the 40th cycle despite a slight increase in the primary stage (Figure S8a). Their corresponding overpotentials are ∼40 mV with large gaps among plating/stripping profiles, higher than those of the PGZ cell (Figure S8b). This phenomenon is ascribed to unstable SEI for the PPP cell, suggesting that PPP fails to effectively passivate the lithium anode and hardly hinders the occurrence of the continuous side reactions between the Li metal and the electrolyte.[36] The ionic resistances at varying temperatures are shown in Figures 3f and S9. According to eq 1, the corresponding ionic conductivity can be calculated, and the relationships between ionic conductivity and thermodynamic temperature are depicted in Figure 3g. Intriguingly, PGZ has a high ionic conductivity of $6.3 \times 10^{-4}$ S cm$^{-1}$ at 20 °C, which meets the requirement of normal operation for solid-state batteries. Astonishingly, it still possesses $2 \times 10^{-4}$ S cm$^{-1}$ at −20 °C. PDOL/crystalline ZIF (PCZ) was also compared, displaying a low ionic conductivity of only $3 \times 10^{-4}$ S cm$^{-1}$ at 20 °C (Figure S9b). By contrast, the ionic conductivity of PPP with the same amount of precursors decreases to $1.5 \times 10^{-5}$ (−20 °C) from $1.3 \times 10^{-4}$ S cm$^{-1}$ (20 °C). This conductivity discrepancy, especially at low temperatures, probably originates from the fast ion-transportation property induced by the grain-boundary-free and isotropic nature of glassy ZIF-62,[24,37] and the new interphase formed between glassy ZIF-62 and PDOL at the premise of their equal precursor amount of the polymer.[5] PGZ has lower activation energy (e.g., 0.052 eV) of Li$^+$ migration in comparison with PPP (e.g., 0.114 eV;

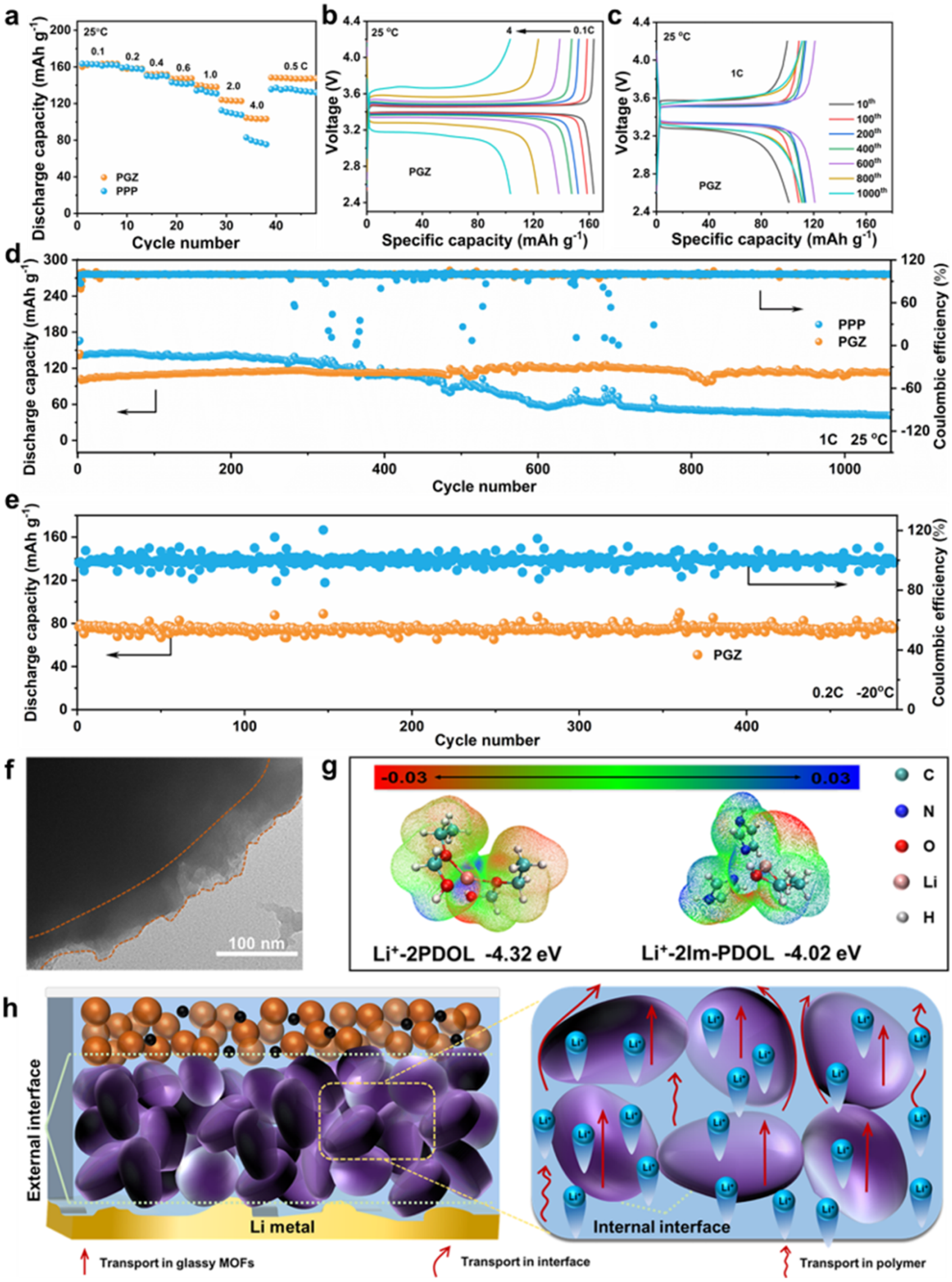

**Figure 5.** (a) Rate performance and (d) cycling stability of LFP|PGZ|Li and LFP|PPP|Li full cells. (b, c) Charge/discharge profiles of LFP|PGZ|Li cells at various current densities and 1C, respectively. (e) Cycling stability of LFP|PGZ|Li cells at −20 °C. (f) TEM image of PGZ. (g) Theoretical calculation of the binding energies of Li with 2PDOL and PDOL−2Im. (h) Illustration of the fast Li$^+$ transport mechanism in PGZ.

Figure 3g) calculated by the Arrhenius equation in eq 2. The stable electrochemical window of PGZ was measured and ranged from 2.5 to 4.6 V via the linear sweeping voltammetry (LSV) approach (Figure 3h), implying the prominent electrochemical stability of PGZ.

A high ion transference number (TN) can markedly reduce the concentration polarization. As described in Figures 4a,b and S10, PGZ has a higher TN value (0.63) than PPP (0.57) and PCZ (0.56). One of the main reasons for triggering the interior short circuit of batteries is Li dendrites, produced by local uneven electric and ionic fields originating from the differences between the diffusion rate and deposition rate of $Li^+$.[38] Fortunately, bearing polar N species and grain boundary-free with isotropy nature from glassy ZIF-62 and the close interior and exterior contact from PDOL, PGZ can realize fast $Li^+$ flux and uniform distribution, ensuring homogeneous Li deposition and thus avoiding the dendrite growth.[13,39,40] Given the above advantages of PGZ, the Li plating/stripping ability of Li||Li symmetrical cells was investigated at gradient current densities. Evidently, PGZ has lower polarization voltages all the time, from 0.01 to 0.06 mA $cm^{-2}$ (Figure 4c). Especially at 0.08, 0.1, and 0.5 mA $cm^{-2}$, Li|PGZ|Li has polarization voltages of only 47, 87, and 280 mV correspondingly, whereas Li|PPP|Li exhibits higher voltages of 71, 89, and 477 mV under the same conditions (Figure 4c). To further assess the interfacial stability, the galvanostatic cycling of Li||Li symmetrical cells was examined. Despite fluctuating voltage over the initial 300 h, Li||Li cells deliver relatively steady cycling for another 1500 h with a polarization voltage of 148.8 mV at 0.3 mA $cm^{-2}$ (Figure 4d). In stark contrast, Li|PPP|Li shows higher polarization voltages over 800 mV after 180 h and short circuits after 252 h under the same test conditions. After cycling, the Li metal anode in the Li|PGZ|Li cell exhibits a smooth surface without dendrites, whereas the counterpart in the Li|PPP|Li cell is rather coarse with pores induced by nonuniform Li deposition (Figure 4e,f). These results further confirm that PGZ has excellent interfacial stability and compatibility with the Li metal in comparison with PPP.

In C 1s spectra from the Li anode surface, the peaks located at 286.6 and 288.7 eV are indexed to the C−O−R and O−C−O groups of the SEI layer derived from the $-CH_2CH_2OCH_2O-$ unit of PDOL (Figure 4g). The C 1s peak (292.0 eV) ascribed to $-CF_3$ from LiTFSI is present in the SEI of the Li anode in contact with PGZ while not being present in the counterpart against PPP. The F 1s peaks' area ratio of $A(-CF_3)/A(LiF)$ in SEI against PGZ is 19.6:1, obviously higher than that (e.g., 0.95:1) of SEI toward PPP (Figure 4h). Such a result also suggests that $TFSI^-$ undergoes continuous decomposition in the PPP electrolyte with the Li anode. These F 1s peaks offer only relative amounts of $-CF_3$ and LiF species rather than the real amount of the respective F species. As well known, LiF is beneficial for the stability of SEI and the uniform Li deposition. However, this does not mean that more LiF is better for stable SEI and uniform Li stripping/plating. An appropriate amount of LiF can reduce the diffusion energy barrier of lithium and stabilize SEI, while excessive LiF can increase the interface impedance and polarization of the battery. For PGZ batteries, the introduction of ZIF-62 effectively prevents the excessive formation of LiF, which is conducive to the formation of a more stable solid electrolyte interface layer with proper LiF content. These mean that the SEI film against PPP is not unstable, and parasitic side reactions repeatedly consume LiTFSI,[29] which is consistent with the results of SEM images (Figure 4f). Such a result further illustrates the overwhelming advantages of PGZ over those of PPP.

To validate the PGZ practicability in LMBs, we evaluated the full cell LFP|PGZ|Li ($LiFePO_4$). Rate performance was initially investigated within the range of 0.1−4C (1C = 170 mAh $g^{-1}$). Although LFP|PGZ|Li has approximate capacities with LFP|PPP|Li from 0.1 to 0.4C, the specific capacities of LFP|PGZ|Li are higher than those of LFP|PPP|Li at higher current densities, especially at 4C (e.g., 103 mAh $g^{-1}$ vs 78 mAh $g^{-1}$; Figure 5a). When the current returns to 0.5C, the capacity of LFP|PGZ|Li recovers to 145 mAh $g^{-1}$, indicative of the excellent physicochemical stability of PGZ. Figure 5b depicts that LFP|PGZ|Li still bears a distinct charge/discharge plateau at 4C, while PPP cell has a low capacity with a less obvious plateau under the same conditions (Figure S11), indicating the better fast-charging ability of PGZ over PPP. It could be concluded that the high ion conductivity of PGZ produces a splendid rate performance. Long-term cycling performance is shown in Figure 5c,d. Although the capacity of LFP|PPP|Li is higher in the initial 360 cycles, it decays fast at less than 40 mAh $g^{-1}$. Strikingly, LFP|PGZ|Li basically keeps a stable capacity of 118 mAh $g^{-1}$ and a near Coulombic efficiency of 100% with a few fadings at 1C over 1000 cycles. This vivid contrast is also embodied in galvanostatic charge/discharge profiles (Figures 5c and S12). With the same amount of the liquid electrolyte containing the DOL monomer, the PPP electrolyte has small internal resistance in comparison with the PGZ film due to the lower thickness of 25 $\mu$m for PPP than that of PGZ (∼70 $\mu$m). With the continuous cycling, the low ionic conductivity and the unstable SEI against PPP cause its capacity decay subsequently. As a comparison, PCZ has a low specific capacity of 65 mAh $g^{-1}$ at 1C with markedly fluctuating Coulombic efficiency (Figure S13). At an even higher current density of 2C, the capacity of LFP|PPP|Li fades fast and decreases to 0 mAh $g^{-1}$ after 20 cycles (Figure S14). In stark contrast, LFP|PGZ|Li delivers an initial capacity of 101 mAh $g^{-1}$ and maintains at 70 mAh $g^{-1}$ at 2 C after 800 cycles. The charge/discharge curves of LFP|PGZ|Li also reveal overwhelming cycling capacity at a high current density (Figure S15). Furthermore, the comprehensive cycling performance surpasses some of the earlier reports (Figure S16). To examine the thermal adaptability of PGZ, LFP|PGZ|Li was carried out in a galvanostatic cycling test at various temperatures from 40 to −20 °C (Figure S17). LFP|PGZ|Li delivers 160 mAh $g^{-1}$ at 0.2C and 40 °C, and its capacity decreases with the declining temperature. The energy density of LFP|PGZ|Li is 367.57 Wh $kg^{1-}$ based on the cathode (at 0.2 and 20 °C). At −20 °C, LFP|PGZ|Li still delivers 70 mAh $g^{-1}$, implying a wide working temperature range. As for long-cycling performance at low temperature, LFP|PGZ|Li exhibits a stable capacity of 75 mAh $g^{-1}$ for 480 cycles at 0.2 and −20 °C (Figures 5e and S18). Such superior low-temperature cycling performance is attributed to the prominent ionic conductivity of PGZ. When the cathodic loading is 12.1 mg $cm^{-2}$, Li|PGZ|LFP delivers a high capacity of 140 mAh $g^{-1}$ at 0.1C for 100 cycles (Figure S19), demonstrating the commercial potential of PGZ. High-voltage NCM 811 as the cathode paired with Li is also investigated. NCM811|PGZ|Li can run for 60 cycles at 0.5 C with 198 mAh $g^{-1}$ and the overlapping charge/discharge profiles (Figure S20).

In order to probe the mechanism of the performance enhancement of ZIF-62 glass, experimental evidence and theoretical calculations are analyzed in depth. As shown in Figure 5f, the formed interphase with continuous and intimate contact is clearly observed outside the glassy ZIF-62 particle, which is derived from the intensive interaction between glassy ZIF-62 and PDOL. According to DFT calculation results, the binding energy of Li-imidazolate is 2.28 eV, lower than that of Li-PDOL (2.60 eV; Figure S21). Additionally, the binding energy of $Li^+$ in the interphase (4.02 eV; composed of imidazolate and PDOL) is lower than that of PDOL (4.32 eV; Figure 5g). These further illustrate that glassy ZIF-62 weakens the $Li^+$ coordination and solvation from PDOL. Hence, the formed interphase is more conducive to the dissociation and conduction of $Li^+$, indictive of the lower resistance and good rate performance of PGZ.[41,42] All in all, the introduction of glassy ZIF-62 combined with PDOL markedly enhances the battery performance as mentioned above. Figure 5h summarizes the mechanism of PGZ boosting the comprehensive electrochemical performance. The integration of PDOL through in situ polymerization stuffs the voids among MOF glass particles and the concave surface between the electrolyte and the electrode, thus optimizing the internal and external interfaces of PGZ. Such structured hybrid SSE is a continuous heterophase for uninterrupted ion migration by glassy MOF and amorphous molecular chains of PDOL. Additionally, the interior interface between glassy ZIF-62 and PDOL provides the extra pathways for ion transport apart from MOF glass and polymer phases.[43] Combined with the above merits, the PGZ composite electrolyte inherits robust dendrite prohibition of glassy MOFs stemming from their rigidity and abundant groups containing N species.

## 3. CONCLUSIONS

In conclusion, we report an outstanding quasi-solid-state composite electrolyte PGZ through in situ polymerization. Combined with the merits of grain-boundary-free and isotropic properties ascribed to MOF glass and the flexibility of PDOL, PGZ delivers high ion conductivity, robust dendrite prohibition, and low interfacial resistance in batteries. Impressively, our proposed PGZ runs for 1800 h at 0.3 mA $cm^{-2}$, and no dendrites in the symmetric cell Li|PGZ|Li were verified by plating/stripping tests. Full cells exhibit a stable cycling test over 1000 cycles at 1C with a stable capacity of 118 mAh $g^{-1}$, outperforming most of the previously reported composite electrolytes. PGZ also presents outstanding low-temperature cycling performance and flame retardance. Therefore, our finding demonstrates that the PDOL/glassy MOF electrolyte prepared via in situ polymerization shows great potential as a solid-state electrolyte and offers promising solutions for safe and high-performance quasi-solid-state batteries.

## 4. EXPERIMENTAL SECTION

**4.1. Materials Synthesis.** ZIF-62(Zn,Co) was synthesized through the solvothermal method at 130 °C for 5 days, and the precursor solution was composed of $Zn(NO_3)_2 \cdot 6H_2O$(99.9%), $Co(NO_3)_2 \cdot 6H_2O$(99.9%), imidazole, and benzimidazole in a mol ratio of 1:1:27:3 and dissolved in 50 mL of N,N-dimethylformamide solvent. The purple deposit was filtered and washed three times with ethanol. The purple product was heated at 460 °C in an Ar atmosphere and cooled to room temperature. Finally, glassy ZIF-62 (G-ZIF-62) was achieved.

**4.2. Characterization.** X-ray diffraction (XRD) patterns were collected on an Empyrean (PANalytical) diffractometer (Cu K$\alpha$ radiation, 0.15406 nm). The porosity was determined by the $N_2$ adsorption/desorption test on an ASiQwin (Quantachrome) instrument. Brunauer−Emmett−Teller (BET) theory was employed to calculate the specific surface area. Degassing conditions were 200 °C temperature for 12 h. The morphology investigation was carried out on a Zeiss Gemini 1530 scanning electron microscope (SEM) equipped with an energy dispersive spectra (EDS) analyzer. Fourier transform infrared spectroscopy (FTIR) data were collected on a Bruker VERTEX 70. Differential scanning calorimetry (DSC) was conducted on a NETZSCH STA 409PC/PG from room temperature to 435 °C. The samples were heated at a rate of 10 °C $min^{-1}$ to the target temperature during the first scan. After the sample was cooled to room temperature, the second upscan was performed using the same procedure as the first time. Thermogravimetric analysis (TGA) was carried out in an argon atmosphere by a ramping rate of 10 °C $min^{-1}$. NMR analysis was performed on a Mercury VX 300 instrument by dissolving DOL and PDOL in dimethyl sulfoxide-d6 (99.9 atom % D, Sigma-Aldrich). GPC was conducted in tetrahydrofuran at an elution rate of 1.0 mL $min^{-1}$ under a Waters Associates GPC system equipped with a Waters 1515 high-performance liquid chromatography pump and an interferometric UV absorption detector.

**4.3. Solid-State Electrolyte Film Preparation.** PGZ was composed of G-ZIF-62. Poly(tetrafluoroethylene) (PTFE) emulsion was used to fabricate solid-state electrolyte film with a thickness of 70 $\mu$m by the rolling approach and cut into a disk with a diameter of 19 mm. Subsequently, the as-obtained film was dried at 80 °C in a vacuum oven for 12 h.

**4.4. Cathode Preparation.** $LiFePO_4$/NCM811, Super P, and polyvinylidene difluoride (PVDF) as a binder in a weight ratio of 8:1:1 in *N*-methyl-pyrrolidone (NMP) were mixed into a slurry and coated on an aluminum foil. The coated foil was dried in a vacuum oven at 80 °C for 12 h and then cut into a round electrode with a diameter of 10 mm. The mass loading of $LiFePO_4$/NCM811 on each disk was ~2.2 mg $cm^{-2}$. A high-loading cathode was also constructed using this method.

**4.5. Battery Assembly.** A 1,3-dioxane (DOL) monomer solution (solution A) containing LiTFSI (1 M) and a proper amount of FEC was stored in a bottle. $LiPF_6$ (3 wt %) as an initiator was dissolved in propylene carbonate (PC) in another bottle (solution B). A certain amount of solution A was added to solution B and fully mixed with a volume ratio of 20 (DOL):7(PC):3(FEC). The mixture (30 $\mu$L) was dropped on a ZIF-62 glass film when cells were assembled. The in situ polymerization occurs at room temperature in the cells. The formed quasi-solid-state electrolyte is denoted PGZ. As a control group, the same amount of the precursor was added to the propylene (PP) separator (denoted PPP). A lithium plate and a $LiFePO_4$ cathode were the anode and cathode, respectively. The thickness of the metal negative electrode used was 400 $\mu$m, and the diameter was 15 mm. All operations were operated in a glovebox in an Ar-filled glovebox with oxygen and moisture concentrations kept below 0.1 ppm. The cycling stability and rate capability of Li||LFP (2.5 and 4.2 V) batteries were evaluated using the battery testing system (CT2001A, LANHE).

**4.6. Electrochemical Characterization.** *4.6.1. Ionic Conductivity.* The ionic conductivity was determined in the configuration of ss|QSSE|ss (stainless steel). The alternating current (AC) impedance investigation was carried out on a Corrtest workstation within a frequency range from 1 MHz to 1 Hz. EIS data were collected from −20 to 40 °C. The ionic conductivity, $\sigma$, was calculated using

$$\sigma = l/(RA) \tag{1}$$

where $l$ is the thickness of the QSSEs, $A$ is the contact area between QSPEs and SS, and $R$ is the resistance measured. The temperature-dependent ionic conductivity of QSSE could be fitted with the following Arrhenius equation

$$\log(\sigma) = -E_a/(2.303RT) + C \tag{2}$$

where $E_a$ is the activation energy, $R$ is the molar gas constant, $T$ is the absolute temperature, and $C$ is a constant.

*4.6.2. Electrochemical Window Determination.* Linear scanning voltammetry (LSV) measurements were conducted in the configuration of a Li|QSSEs|SS asymmetric cell within a voltage range of 0−6 V (vs Li/$Li^+$) at 0.5 mV $s^{-1}$.

*4.6.3. Ion Transference Number.* The configuration of Li|QSSEs|Li in the CR2025 coin cell was employed to measure the $Li^+$ transference number ($t_{Li^+}$) by combining an AC impedance measurement and a direct current (DC) potentiostatic polarization measurement. The EIS was measured between 1 MHz and 0.1 Hz before and after the DC polarization (a voltage amplitude of 10 mV).

*4.6.4. Tests of Dendrite Inhibition.* To evaluate the electrochemical stability between Li and QSPE, Li||Cu and Li||Li CR2032 coin cells with QSSEs were assembled and further evaluated at 0.2 mA $cm^{-2}$ and 0.2 mAh $cm^{-2}$ for 100 cycles.

**4.7. Theoretical Calculations.** All calculations were performed by using the Gauss 16 package. Among them, the solvation structure optimization, frequency analysis, and single-point energy calculation of $Li^+$ were all calculated using the combination of B3LYP and the 6-311 + G (d, p) basis set. The 6-31 G (d, p) basis set was used for small atoms. Only the most stable and optimized structures were presented in this work.

## ASSOCIATED CONTENT

### Supporting Information

The Supporting Information is available free of charge at https://pubs.acs.org/doi/10.1021/acsnano.3c11725.

> Additional results including thermogravimetric curve; nitrogen isotherm adsorption curve; $^1H$ NMR; GPC; SEM; AC impedance spectroscopy; battery cycle data; and theoretical calculation results (PDF)

## AUTHOR INFORMATION

### Corresponding Authors

**Guangshen Jiang** − *Key Laboratory of Energy Materials and Electrochemistry Research Liaoning Province, School of Chemical Engineering, University of Science and Technology Liaoning, Anshan 114051, China;* orcid.org/0000-0001-9213-1515; Email: jiangguangshen2009@126.com

**Yanyan Wei** − *Key Laboratory of Rubber-Plastics, Ministry of Education/Shandong Provincial Key Laboratory of Rubber-Plastics, School of Polymer Science and Engineering, Qingdao University of Science & Technology, Qingdao 266000, China*; Email: yanyanwei_article@163.com

**Baigang An** − *Key Laboratory of Energy Materials and Electrochemistry Research Liaoning Province, School of Chemical Engineering, University of Science and Technology Liaoning, Anshan 114051, China;* orcid.org/0000-0001-6111-8166; Email: bgan@ustl.edu.cn

### Authors

**Shouxiang Liu** − *Key Laboratory of Rubber-Plastics, Ministry of Education/Shandong Provincial Key Laboratory of Rubber-Plastics, School of Polymer Science and Engineering, Qingdao University of Science & Technology, Qingdao 266000, China*

**Yimao Wang** − *Key Laboratory of Rubber-Plastics, Ministry of Education/Shandong Provincial Key Laboratory of Rubber-Plastics, School of Polymer Science and Engineering, Qingdao University of Science & Technology, Qingdao 266000, China*

**Chengyang Liu** − *Key Laboratory of Rubber-Plastics, Ministry of Education/Shandong Provincial Key Laboratory of Rubber-Plastics, School of Polymer Science and Engineering, Qingdao University of Science & Technology, Qingdao 266000, China*

**Tongyang Zhang** − *Key Laboratory of Rubber-Plastics, Ministry of Education/Shandong Provincial Key Laboratory of Rubber-Plastics, School of Polymer Science and Engineering, Qingdao University of Science & Technology, Qingdao 266000, China*

Complete contact information is available at:
https://pubs.acs.org/10.1021/acsnano.3c11725

### Author Contributions

G.J. and S.L. designed the experiments. S.L. completed material synthesis and electrochemical testing. Y.W. completed XRD and FTIR testing. C.L. completed NMR and TEM testing. T.Z. completed SEM testing. S.L. wrote the draft. G.J., Y.W., and B.A. revised the paper and supervised and managed the entire experiment.

### Notes

The authors declare no competing financial interest.

## ACKNOWLEDGMENTS

The funding from the National Natural Science Foundation of China (No. 52371224), University of Science and Technology Liaoning Talent Project Grants (6003000341), Fundamental Research Funds in Higher Education of Liaoning (JYTMS20230945), and Shandong Province Science and Technology Small and Medium-Sized Enterprise Innovation Capacity Improvement project (2021TSGC1198) is gratefully acknowledged.

## REFERENCES

(1) Wang, T.; Luo, W.; Huang, Y. Engineering Li metal anode for garnet-based solid-state batteries. *Acc. Chem. Res.* **2023**, *56* (6), 667−676.

(2) Jiang, G.; Han, H.; Zhuang, W.; Xu, X.; Kaskel, S.; Xu, F.; Wang, H. Three-dimensional ordered mesoporous cobalt nitride for fast-kinetics and stable-cycling lithium storage. *J. Mater. Chem. A* **2019**, *7* (29), 17561−17569.

(3) Xu, F.; Qu, C.; Lu, Q.; Meng, J.; Zhang, X.; Xu, X.; Qiu, Y.; Ding, B.; Yang, J.; Cao, F.; et al. Atomic Sn-enabled high-utilization, large-capacity, and long-life Na anode. *Sci. Adv.* **2022**, *8* (19), No. eabm7489, DOI: 10.1126/sciadv.abm7489.

(4) Zheng, J.; Liu, S.; Huang, H.; Zhou, H.; Li, H.; Li, L.; Jiang, G.; Zhang, H.; Geng, X.; An, B.; et al. Heterocyclic polymer supported cathode/Li interface layers to lower the operational temperature of PEO-based Li-batteries. *Nano Energy* **2023**, *118*, No. 108975.

(5) Liang, H.; Wang, L.; Wang, A.; Song, Y.; Wu, Y.; Yang, Y.; He, X. Tailoring practically accessible polymer/inorganic composite electrolytes for all-solid-state lithium metal batteries: A review. *Nano-Micro Lett.* **2023**, *15* (3), 266−297, DOI: 10.1007/s40820-022-00996-1.

(6) Liu, S.; Liu, W.; Ba, D.; Zhao, Y.; Ye, Y.; Li, Y.; Liu, J. Filler-integrated composite polymer electrolyte for solid-state lithium batteries. *Adv. Mater.* **2022**, *35* (2), No. 2110423, DOI: 10.1002/adma.202110423.

(7) Jiang, S.; Lv, T.; Peng, Y.; Pang, H. MOFs containing solid-state electrolytes for batteries. *Adv. Sci.* **2023**, *10* (10), No. 2206887, DOI: 10.1002/advs.202206887.

(8) Ma, N.; Horike, S. Metal-organic network-forming glasses. *Chem. Rev.* **2022**, *122* (3), 4163−4203.

(9) Zhao, R.; Wu, Y. X.; Liang, Z. B.; Gao, L.; Xia, W.; Zhao, Y. S.; Zou, R. Q. Metal-organic frameworks for solid-state electrolytes. *Energy Environ. Sci.* **2020**, *13* (8), 2386−2403.

(10) Bennett, T. D.; Horike, S. Liquid, glass and amorphous solid states of coordination polymers and metal-organic frameworks. *Nat. Rev. Mater.* **2018**, *3* (11), 431−440.

(11) Tao, H.; Bennett, T. D.; Yue, Y. Melt-quenched hybrid glasses from metal-organic frameworks. *Adv. Mater.* **2017**, *29* (20), No. 1601705, DOI: 10.1002/adma.201601705.

(12) Chai, M.; Chen, R.; Xu, K.; Chen, Y.; Ma, S.; Lin, R.; Chen, V.; Hou, J. Ion transport and conduction in metal−organic framework glasses. *J. Mater. Chem. A* **2023**, *11* (38), 20302−20314.

(13) Jiang, G.; Qu, C.; Xu, F.; Zhang, E.; Lu, Q.; Cai, X.; Hausdorf, S.; Wang, H.; Kaskel, S. Glassy metal-organic-framework-based quasi-solid-state electrolyte for high-performance lithium-metal batteries. *Adv. Funct. Mater.* **2021**, *31* (43), No. 2104300, DOI: 10.1002/adfm.202104300.

(14) Zhang, Y.; Liu, Y.; Bao, W.; Zhang, X.; Yan, P.; Yao, X.; Chen, M. Z.; Xie, T. Y.; Cao, L.; Cai, X.; et al. Monolithic titanium alkoxide networks for lithium-ion conductive all-solid-state electrolytes. *Nano Lett.* **2023**, *23* (9), 4066−4073.

(15) Horike, S.; Ma, N.; Fan, Z. Y.; Kosasang, S.; Smedskjaer, M. M. Mechanics, ionics, and optics of metal-organic framework and coordination polymer glasses. *Nano Lett.* **2021**, *21* (15), 6382−6390.

(16) Fonseca, J.; Gong, T.; Jiao, L.; Jiang, H.-L. Metal-organic frameworks (MOFs) beyond crystallinity: amorphous MOFs, MOF liquids and MOF glasses. *J. Mater. Chem. A* **2021**, *9* (17), 10562−10611.

(17) Bao, C.; Zheng, C.; Wu, M.; Zhang, Y.; Jin, J.; Chen, H.; Wen, Z. 12 μm-thick sintered garnet ceramic skeleton enabling high-energy-density solid-state lithium metal batteries. *Adv. Energy Mater.* **2023**, *13* (13), No. 2204028, DOI: 10.1002/aenm.202204028.

(18) Sahore, R.; Armstrong, B. L.; Tang, X.; Liu, C.; Owensby, K.; Kalnaus, S.; Chen, X. C. Role of scaffold architecture and excess surface polymer layers in a 3D-interconnected ceramic/polymer composite electrolyte. *Adv. Energy Mater.* **2023**, *13* (19), No. 2203663, DOI: 10.1002/aenm.202203663.

(19) Su, Y.; Xu, F.; Zhang, X.; Qiu, Y.; Wang, H. Rational design of high-performance PEO/ceramic composite solid electrolytes for lithium metal batteries. *Nano-Micro Lett.* **2023**, *15* (1), No. 82, DOI: 10.1007/s40820-023-01055-z.

(20) Didwal, P. N.; Singhbabu, Y. N.; Verma, R.; Sung, B. J.; Lee, G. H.; Lee, J. S.; Chang, D. R.; Park, C. J. An advanced solid polymer electrolyte composed of poly(propylene carbonate) and mesoporous silica nanoparticles for use in all-solid-state lithium-ion batteries. *Energy Storage Mater.* **2021**, *37*, 476−490.

(21) Pan, J.; Zhang, Y.; Sun, F.; Osenberg, M.; Hilger, A.; Manke, I.; Cao, R.; Dou, S. X.; Fan, H. J. Designing solvated double-layer polymer electrolytes with molecular interactions mediated stable interfaces for sodium ion batteries. *Angew. Chem., Int. Ed.* **2023**, *62* (17), No. 2219000, DOI: 10.1002/anie.202219000.

(22) Zhou, X.; Zhang, B.; Huang, F.; et al. Difunctional MOF for dendrite-free all-solid-state lithium metal batteries by synergistic effect of hydrogen bond and electrostatic interaction. *Nano Energy* **2023**, *108*, No. 108221.

(23) Zhao, Z.; Zhou, X.; Zhang, B.; et al. Regulating Steric Hindrance of porous organic polymers in composite solid-state electrolytes to induce the formation of LiF-rich SEI in Li-ion batteries. *Angew. Chem., Int. Ed.* **2023**, *62* (39), No. e202308738, DOI: 10.1002/anie.202308738.

(24) Wang, M.; Zhao, H.; Du, B.; Lu, X.; Ding, S.; Hu, X. Functions and applications of emerging metal-organic-framework liquids and glasses. *Chem. Commun.* **2023**, *59* (47), 7126−7140.

(25) Qiao, A.; Bennett, T. D.; Tao, H.; Krajnc, A.; Mali, G.; Doherty, C. M.; Thornton, A. W.; Mauro, J. C.; Greaves, G. N.; Yue, Y. A metal-organic framework with ultrahigh glass-forming ability. *Sci. Adv.* **2018**, *4* (3), No. eaao6827, DOI: 10.1126/sciadv.aao6827.

(26) Yan, J.; Gao, C.; Qi, S.; Jiang, Z.; Jensen, L. R.; Zhan, H.; Zhang, Y.; Yue, Y. Encapsulation of nano-Si into MOF glass to enhance lithium-ion battery anode performances. *Nano Energy* **2022**, *103*, No. 107779.

(27) Gao, C.; Jiang, Z.; Qi, S.; Wang, P.; Jensen, L. R.; Johansen, M.; Christensen, C. K.; Zhang, Y.; Ravnsbaek, D. B.; Yue, Y. Metal-organic framework glass anode with an exceptional cycling-induced capacity enhancement for lithium-ion batteries. *Adv. Mater.* **2022**, *34* (10), No. 2110048, DOI: 10.1002/adma.202110048.

(28) Madsen, R. S. K.; Qiao, A.; Sen, J.; Hung, I.; Chen, K.; Gan, Z.; Sen, S.; Yue, Y. Ultrahigh-field (67)Zn NMR reveals short-range disorder in zeolitic imidazolate framework glasses. *Science* **2020**, *367* (6485), 1473−1476.

(29) Yu, J.; Lin, X.; Liu, J.; Yu, J. T. T.; Robson, M. J.; Zhou, G.; Law, H. M.; Wang, H.; Tang, B. Z.; Ciucci, F. In situ fabricated quasi-solid polymer electrolyte for high-energy-density lithium metal battery capable of subzero operation. *Adv. Energy Mater.* **2021**, *12* (2), No. 2102932, DOI: 10.1002/aenm.202102932.

(30) Zhao, Q.; Liu, X.; Stalin, S.; Khan, K.; Archer, L. A. Solid-state polymer electrolytes with in-built fast interfacial transport for secondary lithium batteries. *Nat. Energy* **2019**, *4* (5), 365−373.

(31) Chen, D.; Zhu, M.; Kang, P.; Zhu, T.; Yuan, H.; Lan, J.; Yang, X.; Sui, G. Self-Enhancing gel polymer electrolyte by in situ construction for enabling safe lithium metal battery. *Adv. Sci.* **2022**, *9* (4), No. 2103663, DOI: 10.1002/advs.202103663.

(32) Liu, F. Q.; Wang, W. P.; Yin, Y. X.; Zhang, S. F.; Shi, J. L.; Wang, L.; Zhang, X. D.; Zheng, Y.; Zhou, J. J.; Li, L.; et al. Upgrading traditional liquid electrolyte via in situ gelation for future lithium metal batteries. *Sci. Adv.* **2018**, *4* (10), No. eaat5383, DOI: 10.1126/sciadv.aat5383.

(33) Cho, Y.-H.; Kim, K.; Ahn, S.; Liu, H. K. Allyl-substituted triazines as additives for enhancing the thermal stability of Li-ion batteries. *J. Power Sources* **2011**, *196* (3), 1483−1487.

(34) Xu, M.; Hao, L.; Liu, Y.; Li, W.; Xing, L.; Li, B. Experimental and theoretical investigations of dimethylacetamide (dmac) as electrolyte stabilizing additive for lithium ion batteries. *J. Phys. Chem. C* **2011**, *115* (13), 6085−6094.

(35) Nabipour, H.; Wang, X.; Song, L.; Hu, Y. Organic-inorganic hybridization of isoreticular metal-organic framework-3 with melamine for efficiently reducing the fire risk of epoxy resin. *Composites, Part B* **2021**, *211*, No. 108606.

(36) Xiang, J.; Zhang, Y.; Zhang, B.; Yuan, L.; Liu, X.; Cheng, Z.; Yang, Y.; Zhang, X.; Li, Z.; Shen, Y.; et al. A flame-retardant polymer electrolyte for high performance lithium metal batteries with an expanded operation temperature. *Energy Environ. Sci.* **2021**, *14* (6), 3510−3521.

(37) Lin, R.; Chai, M.; Zhou, Y.; Chen, V.; Bennett, T. D.; Hou, J. Metal-organic framework glass composites. *Chem. Soc. Rev.* **2023**, *52* (13), 4149−4172.

(38) Liu, D. H.; Bai, Z. Y.; Li, M.; Yu, A. P.; Luo, D.; Liu, W. W.; Yang, L.; Lu, J.; Amine, K.; Chen, Z. W. Developing high safety Li-metal anodes for future high-energy Li-metal batteries: strategies and perspectives. *Chem. Soc. Rev.* **2020**, *49* (15), 5407−5445.

(39) Miao, X.; Wang, P.; Sun, R.; Li, J.; Wang, Z.; Zhang, T.; Wang, R.; Li, Z.; Bai, Y.; Hao, R.; et al. Liquid metal-organic frameworks in-situ derived interlayer for high-performance solid-state Na-metal batteries. *Adv. Energy Mater.* **2021**, *11* (47), No. 2102396, DOI: 10.1002/aenm.202102396.

(40) Zhuang, R.; Zhang, X.; Qu, C.; Xu, X.; Yang, J.; Ye, Q.; Liu, Z.; Kaskel, S.; Xu, F.; Wang, H. Fluorinated porous frameworks enable robust anode-less sodium metal batteries. *Sci. Adv.* **2023**, *9* (39), No. eadh8060, DOI: 10.1126/sciadv.adh8060.

(41) Guo, D.; Shinde, D.; Shin, W.; Abou-Hamad, E.; Emwas, A.; Lai, Z.; Manthiram, A. Foldable solid-state batteries enabled by electrolyte mediation in covalent organic frameworks. *Adv. Mater.* **2022**, *34* (23), No. 2201410, DOI: 10.1002/adma.202201410.

(42) Liu, Q.; Yang, L.; Mei, Z.; An, Q.; Zeng, K.; Huang, W.; Wang, S.; Sun, Y.; Guo, H. Constructing host−guest recognition electrolytes promotes the $Li^+$ kinetics in solid-state batteries. *Energy Environ. Sci.* **2024**, *17* (2), 780−790, DOI: 10.1039/D3EE03283C.

(43) Liu, M.; Ganapathy, S.; Wagemaker, M. A direct view on Li-ion transport and Li-metal plating in inorganic and hybrid solid-state electrolytes. *Acc. Chem. Res.* **2022**, *55* (3), 333−344.